



VERITAS and Fermi-LAT Constraints on the Gamma-Ray Emission from Superluminous Supernovae SN2015bn and SN2017egm

A. Acharyya¹ , C. B. Adams² , P. Bangale³ , W. Benbow⁴ , J. H. Buckley⁵ , M. Capasso⁶ , V. V. Dwarkadas⁷ , M. Errando⁵ , A. Falcone⁸ , Q. Feng⁶ , J. P. Finley⁹ , G. M. Foote³ , L. Fortson¹⁰ , A. Furniss¹¹ , G. Gallagher¹² , A. Gent¹³ , W. F. Hanlon⁴ , O. Hervet¹⁴ , J. Holder³ , T. B. Humensky¹⁵ , W. Jin¹ , P. Kaaret¹⁶ , M. Kertzman¹⁷ , M. Kherlakian¹⁸ , D. Kieda¹⁹ , T. K. Kleiner¹⁸ , S. Kumar²⁰ , M. J. Lang²¹ , M. Lundy²⁰ , G. Maier¹⁸ , C. E. McGrath²² , J. Millis²³ , P. Moriarty²¹ , R. Mukherjee⁶ , M. Nieves-Rosillo¹⁸ , S. O'Brien²⁰ , R. A. Ong²⁴ , S. R. Patel¹⁸ , K. Pfrang¹⁸ , M. Pohl²⁵ , E. Pueschel¹⁸ , J. Quinn²² , K. Ragan²⁰ , P. T. Reynolds²⁶ , D. Ribeiro²⁷ , E. Roache⁴ , J. L. Ryan²⁴ , I. Sadeh¹⁸ , M. Santander¹ , G. H. Sembroski⁹ , R. Shang²⁴ , M. Spletstoesser¹⁴ , D. Tak¹⁸ , J. V. Tucci²⁸ , A. Weinstein²⁹ , D. A. Williams¹⁴

(VERITAS collaboration)³³,

B. D. Metzger^{27,30} , M. Nicholl³¹ , and I. Vurm³²

¹ Department of Physics and Astronomy, University of Alabama, Tuscaloosa, AL 35487, USA; d.ribeiro@columbia.edu

² Physics Department, Columbia University, New York, NY 10027, USA

³ Department of Physics and Astronomy and the Bartol Research Institute, University of Delaware, Newark, DE 19716, USA

⁴ Center for Astrophysics — Harvard & Smithsonian, Cambridge, MA 02138, USA

⁵ Department of Physics, Washington University, St. Louis, MO 63130, USA

⁶ Department of Physics and Astronomy, Barnard College, Columbia University, NY 10027, USA

⁷ Department of Astronomy and Astrophysics, University of Chicago, Chicago, IL 60637, USA

⁸ Department of Astronomy and Astrophysics, 525 Davey Lab, Pennsylvania State University, University Park, PA 16802, USA

⁹ Department of Physics and Astronomy, Purdue University, West Lafayette, IN 47907, USA

¹⁰ School of Physics and Astronomy, University of Minnesota, Minneapolis, MN 55455, USA

¹¹ Department of Physics, California State University—East Bay, Hayward, CA 94542, USA

¹² Department of Physics and Astronomy, Ball State University, Muncie, IN 47306, USA

¹³ School of Physics and Center for Relativistic Astrophysics, Georgia Institute of Technology, 837 State Street NW, Atlanta, GA 30332-0430, USA

¹⁴ Santa Cruz Institute for Particle Physics and Department of Physics, University of California, Santa Cruz, CA 95064, USA

¹⁵ Department of Physics, University of Maryland, College Park, MD 20742, USA

¹⁶ Department of Physics and Astronomy, University of Iowa, Van Allen Hall, Iowa City, IA 52242, USA

¹⁷ Department of Physics and Astronomy, DePaul University, Greencastle, IN 46135-0037, USA

¹⁸ DESY, Platanenallee 6, D-15738 Zeuthen, Germany

¹⁹ Department of Physics and Astronomy, University of Utah, Salt Lake City, UT 84112, USA

²⁰ Physics Department, McGill University, Montreal, QC H3A 2T8, Canada

²¹ School of Physics, National University of Ireland Galway, University Road, Galway, Ireland

²² School of Physics, University College Dublin, Belfield, Dublin 4, Ireland

²³ Department of Physics and Astronomy, Ball State University, Muncie, IN 47306, USA and Department of Physics, Anderson University, 1100 East 5th Street, Anderson, IN 46012, USA

²⁴ Department of Physics and Astronomy, University of California, Los Angeles, CA 90095, USA

²⁵ Institute of Physics and Astronomy, University of Potsdam, 14476 Potsdam-Golm, Germany and DESY, Platanenallee 6, D-15738 Zeuthen, Germany

²⁶ Department of Physical Sciences, Munster Technological University, Bishopstown, Cork, T12 P928, Ireland

²⁷ Department of Physics, Columbia University, New York, NY 10027*, USA

²⁸ Department of Physics, Indiana University-Purdue University Indianapolis, Indianapolis, IN 46202, USA

²⁹ Department of Physics and Astronomy, Iowa State University, Ames, IA 50011, USA

³⁰ Center for Computational Astrophysics, Flatiron Institute, 162 5th Ave, New York, NY 10010, USA

³¹ Birmingham Institute for Gravitational Wave Astronomy and School of Physics and Astronomy, University of Birmingham, Birmingham B15 2TT, UK

³² Tartu Observatory, University of Tartu, Toravere 61602, Tartumaa, Estonia

Received 2022 June 6; revised 2022 December 21; accepted 2023 January 30; published 2023 March 3

Abstract

Superluminous supernovae (SLSNe) are a rare class of stellar explosions with luminosities ~ 10 – 100 times greater than ordinary core-collapse supernovae. One popular model to explain the enhanced optical output of hydrogen-poor (Type I) SLSNe invokes energy injection from a rapidly spinning magnetar. A prediction in this case is that high-energy gamma-rays, generated in the wind nebula of the magnetar, could escape through the expanding supernova ejecta at late times (months or more after optical peak). This paper presents a search for gamma-ray emission in the broad energy band from 100 MeV to 30 TeV from two Type I SLSNe, SN2015bn, and SN2017egm, using observations from Fermi-LAT and VERITAS. Although no gamma-ray emission was detected from either source, the derived upper limits approach the putative magnetar's spin-down luminosity. Prospects are

³³ <https://veritas.sao.arizona.edu>



explored for detecting very-high-energy (VHE; 100 GeV–100 TeV) emission from SLSNe-I with existing and planned facilities such as VERITAS and CTA.

Unified Astronomy Thesaurus concepts: Shocks (2086); Gamma-rays (637); Particle astrophysics (96); Supernovae (1668); Magnetars (992); Millisecond pulsars (1062); Rotation powered pulsars (1408)

1. Introduction

The recent growth of sensitive optical time-domain surveys has revealed and expanded exciting new classes of stellar explosions. These include superluminous supernovae, which can be up to 10–100 times more luminous than ordinary massive star explosions (e.g., Quimby et al. 2011; Howell et al. 2013; Inserra et al. 2013; Nicholl et al. 2013; De Cia et al. 2018; Lunnan et al. 2018; Quimby et al. 2018; see Gal-Yam 2019 for a recent review). Conventionally, the optical emission from most core-collapse supernovae is powered by the radioactive decay of ^{56}Ni (Type Ib/c) and by thermal energy generated via shock heating of the stellar envelope (Type IIL, Iip). However, the peak luminosities of SLSNe greatly exceed the luminosity expected from those conventional mechanisms, and the origin of the energy is still debated.

A popular model for powering the time-dependent emission of SLSNe, particularly the hydrogen-poor Type I class (SLSN-I), involves energy input from a young central engine, such as a black hole or neutron star, formed in the explosion. For example, the accretion onto the compact object from bound debris of the explosion could power an outflow that heats the supernova ejecta from within (Woosley & Heger 2012; Quataert & Kasen 2012; Margalit & Metzger 2016; Moriya et al. 2018). Alternatively, the central engine could be a strongly magnetized neutron star with a millisecond rotation period, whose rotationally powered wind provides a source of energetic particles that heat the supernova ejecta (Kasen & Bildsten 2010; Woosley 2010; Dessart et al. 2012; Metzger et al. 2015; Sukhbold & Woosley 2016). The magnetar³⁴ model provides a good fit to the optical light curves of most SLSNe-I (Inserra et al. 2013; Nicholl et al. 2017b). Furthermore, analyses of the nebular spectra of hydrogen-poor SLSNe (Jerkstrand et al. 2017; Nicholl et al. 2019) and Type Ib SNe (Milisavljevic et al. 2018) support the presence of a persistent central energy source, consistent with an energetic neutron star.

The details of how the magnetar would couple its energy to the ejecta are uncertain. Several models consider that the rotationally powered wind from a young pulsar inflates a nebula of relativistic electron/positron pairs and energetic radiation behind the expanding ejecta (Kotera et al. 2013; Metzger et al. 2014; Murase et al. 2015). At the wind-termination shock, the pairs are heated and radiate X-rays and gamma-rays with high efficiency via synchrotron and inverse-Compton processes. Photons that evade absorption via $\gamma\text{--}\gamma$ pair creation in the nebula can be “absorbed” by the ejecta further out, thermalizing their energy and directly powering the supernova’s optical emission (e.g., Metzger et al. 2014; Vurm & Metzger 2021).

Thermalization of the nebular radiation will be most efficient at early times, when the column through the ejecta shell and

“compactness” of the nebula are at their highest. At these times one would expect the optical light curve to faithfully track the energy input of the central engine. However, as the ejecta expand, the radiation field dilutes and the shell becomes increasingly transparent to high-energy and very-high-energy photons. The increasing transparency, and correspondingly decreasing thermalization efficiency, eventually causes the supernova’s optical luminosity to drop below the rate of energy injection from the central engine (Chen et al. 2015; Wang et al. 2015), with the remaining radiation escaping directly from the nebula as gamma-rays or X-rays (the putative “missing” luminosity).

As the ejecta expand and the spin-down luminosity weakens, the conditions for various processes responsible for photon energy loss change and impact the effective optical depth. Within a few months, the effective optical depth to high-energy (HE; 100 MeV–100 GeV) photons emitted from the central engine nears unity and, at several hundred days, it reaches unity for very-high-energy (VHE; 100 GeV–100 TeV) photons.

Figure 1 shows examples of the effective optical depth through the ejecta for photons of various energies as a function of time. They have been calculated using time-dependent properties for the supernova ejecta and radiation field motivated by the observations of SN2015bn and SN2017egm, both particularly well-studied SLSNe-I explored in Vurm & Metzger (2021).

The dominant processes involved in the calculation of the gamma-ray optical depth include photon–matter and photon–photon interactions, particularly pair production on the nuclei and soft radiation fields in the ejecta. An accurate treatment considering the radiation transport is discussed in depth in Vurm & Metzger (2021). The standard version of the magnetar model (Kasen & Bildsten 2010; Woosley 2010; Nicholl et al. 2017b) does not consider this time-dependent calculation and relies on constant effective opacities to optical and high-energy photons. Figure 1 provides a useful guiding timescale for when to consider gamma-ray emission at various energies, calculated with the model in Vurm & Metzger (2021) using the ejecta properties fit to the optical data in Table 1.

Given its comparatively nearby distance at $z=0.1136$, SN2015bn is an excellent candidate event to test the magnetar hypothesis. The optical light curve shows a steepening from $\propto t^{-2}$ decay to $\propto t^{-4}$ around ~ 200 days (Nicholl et al. 2018). This behavior is consistent with a leakage of high-energy radiation from a magnetar nebula (Nicholl et al. 2018). A deep search in the $\sim 0.1\text{--}10$ keV X-ray band resulted in nondetections (Bhimbhakhadi et al. 2018), eliminating the possibility that leakage from the nebula occurs in the softer X-ray bands.

Margutti et al. (2018) present a similar search for late-time X-ray emission from a larger sample of SLSNe-I, mostly resulting in upper limits; however, see Levan et al. (2013) for an X-ray detection of the SLSN-I SCP 06F6 that could still support the magnetar hypothesis. X-ray nondetections are not surprising, because the ejecta are likely to still be opaque in the $\lesssim 10$ keV band due to photoelectric absorption in the hydrogen-poor ejecta (Margalit et al. 2018a). Intriguingly, Eftekhari et al. (2019)

³⁴ To remain consistent with the SLSNe literature, the term magnetar is used throughout this paper. Magnetars generally have large dipole magnetic fields $B \simeq 1 \times 10^{13}$ G to 1×10^{15} G with a rotation period of a few seconds. In the case of the SLSN magnetar model, the radiation is extracted from the rotational energy of the young millisecond pulsars, but with large magnetic fields characteristic of magnetars.

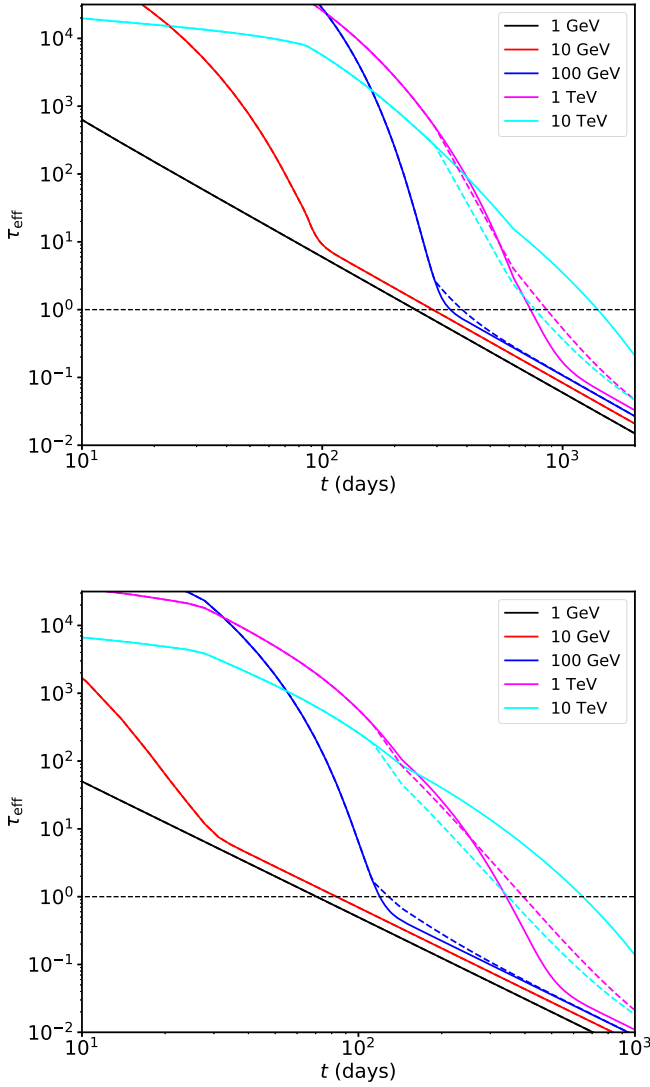


Figure 1. Optical depth at different photon energies as a function of time, calculated for ejecta properties (mass M_{\odot} , mean velocity, etc.) derived from observations of SN2015bn (Nicholl et al. 2018) and SN2017egm (Nicholl et al. 2017a) shown in Table 1. Top: SN2015bn. Bottom: SN2017egm. The horizontal dotted line represents $\tau_{\text{eff}} = 1$. The cross sections for photon–photon and photon–matter pair production opacities are taken from Zdziarski & Svensson (1989). The solid lines correspond to target blackbody radiation temperature $T_{\text{eff}} = (L_{\text{opt}}/4\pi R^2)^{1/4}$, where L_{opt} and R are the optical luminosity and ejecta radius, respectively. The dashed lines are computed with a temperature floor of $T = 4000$ K, to mimic the approximate spectrum in the nebular phase. Below ~ 10 GeV, the opacity is dominated by photon–matter pair production at all times. Above 100 GeV, pair production on the thermal target radiation field dominates up to a few years.

detected radio emission from the location of the SLSN PTF10hgi at 7.5 yr after the explosion and argued that the emission could be synchrotron emission from an engine-powered nebula.

Some effort has been underway to search for nebular leakage in the gamma-ray band. Renault-Tinacci (2018) obtained upper limits on the 0.6–600 GeV luminosities from SLSNe by a stacked analysis of 45 SLSNe with Fermi-LAT. The majority of their sample were SLSNe-I, the most likely class to be powered by a central engine; however the results were dominated by a single, extremely close Type II event (SLSN-II), CSS140222. Hydrogen-rich SLSNe make up the Type II class (SLSN-II), which are suggested to be powered by the

Table 1
Properties of the SLSNe Considered in this Paper

Parameter	(Unit)	SN2015bn	SN2017egm
R.A.	°	173.4232	154.7734
decl.	°	0.725	46.454
z	...	0.1136	0.0310
t_0^a	MJD	57014	57896
t_{pk}^b	MJD	57100	57922
P_0^c	ms	$2.50^{+0.29}_{-0.17}$	$5.83^{+0.73}_{-0.70}$
B^d	10^{14} G	$0.26^{+0.07}_{-0.05}$	$0.94^{+0.13}_{-0.16}$
M_{ej}^e	M_{\odot}	$10.8^{+0.83}_{-1.34}$	$2.99^{+0.30}_{-0.23}$
κ^f	$\text{cm}^2 \text{g}^{-1}$	$0.18^{+0.01}_{-0.02}$	$0.12^{+0.04}_{-0.06}$
v_{ej}^h	10^8 cm s^{-1}	$5.68^{+0.16}_{-0.14}$	$10.3^{+0.35}_{-0.27}$
κ_{γ}^i	$\text{cm}^2 \text{g}^{-1}$	$0.008^{+0.01}_{-0.01}$	$0.080^{+0.15}_{-0.06}$
M_{NS}^j	M_{\odot}	$1.84^{+0.28}_{-0.23}$	$1.57^{+0.25}_{-0.29}$

Notes. The quantities P_0 , B , M_{ej} , κ , E_{SN} , v_{ej} , κ_{γ} and M_{NS} were obtained from a best-fit to the UVOIR supernova light curves, with errors found in Nicholl et al. (2017a), (2017b).

^a Epoch of explosion.

^b Epoch of optical flux peak.

^c Initial spin period.

^d Magnetic field strength of magnetar.

^e Total mass.

^f Effective opacity.

^g Kinetic energy.

^h Mean velocity of supernova ejecta.

ⁱ Gamma-ray effective opacity.

^j Neutron star mass.

interaction of the circumstellar medium with the supernova ejecta. Nevertheless, even with CSS140222 included, the upper limits are at best marginally constraining on the inferred missing luminosity.

In this paper, the search is expanded to gamma-ray emission from SLSNe-I in the HE to VHE bands using the Fermi Gamma-Ray Space Telescope and the ground-based VERITAS observatory. In particular, observations of SN2015bn and SN2017egm are presented here. SN2017egm is the closest SLSN-I to date in the Northern Hemisphere at $z = 0.0310$ (Bose et al. 2017; Nicholl et al. 2017a). Observations of young supernovae with gamma-ray telescopes have been few, with no detections so far. Some tantalizing candidates like iPTF14hls and SN 2004dj have been explored with Fermi-LAT but are unconfirmed due to large localization regions overlapping with other gamma-ray candidates (Yuan et al. 2018; Xi et al. 2020). MAGIC carried out observations of a Type I SN (Ahn et al. 2017). HESS observed a sample of core-collapse SNe (Abdalla et al. 2019), and later obtained upper limits on SN 1987A (The H.E.S.S. Collaboration 2015). Our observations are the first of superluminous supernovae.

Throughout this paper, a flat Λ CDM cosmology is used, with $H_0 = 67.7 \text{ km s}^{-1} \text{ Mpc}^{-1}$, $\Omega_M = 0.307$, and $\Omega_{\Lambda} = 0.6911$ (Planck Collaboration et al. 2016). The corresponding luminosity distances to SN2015bn and SN2017egm are 545.37 Mpc ($z = 0.1136$) (Nicholl et al. 2016a) and 139.29 Mpc ($z = 0.0310$) (Bose et al. 2017).

2. Observations and Methods

The superluminous supernovae SN2015bn and SN2017egm were observed with Fermi-LAT and VERITAS during

2015–2016 and 2017–2020, respectively. SN2015bn is a SLSN-I explosion from 2014 December 23 (MJD 57014) and it peaked optically on 2015 March 19 (MJD 57100) Nicholl et al. (2016b). SN2017egm is a SLSN-I explosion from 2017 May 23 (MJD 57896) and it peaked optically on 2017 June 18 (MJD 57922) Bose et al. (2017). Some properties of the SLSNe are given in Table 1. Details regarding the optical, Fermi-LAT and VERITAS observations and the data-analysis methods are below.

2.1. Fermi-LAT

The Large Area Telescope (LAT) on board the Fermi satellite has operated since 2008 (Atwood et al. 2009). It is sensitive to photons between ~ 20 MeV and ~ 300 GeV and has an $\sim 60^\circ$ field of view, enabling it to survey the entire sky in about 3 hours.

The data were analyzed using the publicly available Fermi-LAT data with the `Fermitools` suite of tools provided by the Fermi Science Support Center (FSSC). Using the `Fermipy` analysis package (Wood et al. 2017),³⁵ the data were prepared for a binned likelihood analysis in which a spatial spectral model is fit over the energy bins. The data were selected using the `SOURCE` class of events, which are optimized for point-source analysis, within a region of 15° radius from the analysis target position. Due to the effect of the Earth, a 90° zenith angle cut was applied to remove any external background events. The standard background models were applied to the test model, incorporating an isotropic background and a galactic diffuse emission model without any modifications. The standard 4FGL catalog was then queried for sources within the field of view and their default model parameters Abdollahi et al. (2020).

Additional putative point sources were added to each field of view as needed to support convergence of the fit. These sources were added for all analysis timescales. This process continued until the distribution of test statistics for the field of view was Gaussian with standard deviation near 1 and mean centered at 0, and the residual maps were near uniformly 0 without strong features. These conditions indicate the appropriate coverage of spectral sources within the analysis was reached and no putative sources are missing. The fitting process is performed in discrete energy bins while optimizing the spectral shape, but the distribution of test statistics is evaluated with the stacked data spanning the full energy range. With the improvements to Fermi-LAT low-energy sensitivity in PASS8 reconstruction, the low-energy bin covering 100–612 MeV was also added.

In the case of both SN2015bn and SN2017egm, the data were fitted with a power-law spectral model, $N(E) = N_0 E^\Gamma$, with a free prefactor and a fixed photon index Γ of -2.0 . From the fit, the reported flux upper limit was found using a 95% confidence level with the bounded Rolke method (Rolke et al. 2005). In all cases reported here, the upper limit reported is the integral energy flux, integrated over the energy ranges described for each case, which has units of $\text{MeV cm}^{-2} \text{s}^{-1}$. This flux is converted to luminosity with the adopted distance for each event.

SN2015bn was observed from 2014 December 23 to 2018 March 23. This observation period begins after the explosion, and is binned in a few windows to account for the absorption of low-energy gamma-rays by the ejecta at early times (Figure 1). The first ~ 90 days is observed to make sure there is no early

emission during the expected absorption period. The data were thereafter binned in time intervals of six months to maximize observation depth and sensitivity to time-dependent variation. SN2017egm was observed 2017 May 23 to 2020 August 21. Again, this period covers the 3.5 yr from the discovery date, starting with ~ 90 days after the explosion and split into six 6 month bins thereafter. The 3.5 yr observation period is selected to cover approximately 1000 days after the explosion. After this period, it is expected that the predicted luminosity will have decreased below the Fermi-LAT detectable limit.

SN2015bn is within 5° of the Sun each year in August, so a one-month time cut is applied to each relevant time bin (to cover an $\sim 15^\circ$ radius field of view). SN2017egm is not near the path of the Sun, so this cut was not applied.

2.2. Veritas

The Very Energetic Radiation Imaging Telescope Array System (VERITAS) is an imaging atmospheric cherenkov telescope (IACT) array at the Fred Lawrence Whipple Observatory (FLWO) in southern Arizona, USA (Weekes et al. 2002; Holder et al. 2006). It consists of four 12 m telescopes separated by approximately 100 m, and the observatory is sensitive to photons within the energy range ~ 100 GeV to ~ 30 TeV. The instrument has an angular resolution (68% containment) of $\sim 0.1^\circ$ at 1 TeV, an energy resolution of $\sim 15\%$ at 1 TeV, and 3.5° field of view.

VERITAS serendipitously observed SN2015bn for a total of 1.01 hr between 2015 May 7 and 22, approximately 135 days from explosion (49 days from the date of peak magnitude), as a part of an unrelated campaign. Another 1.7 hr were taken between 2016 May 25 and 30. Data were taken in good weather and dark sky conditions. Since SN2015bn was not the target source, its sky position averages 1.4° from the center of the camera.

VERITAS directly observed SN2017egm for 8.7 hr between 2019 March 24 and April 5, under dark sky conditions, as part of a Directors Discretionary Time (DDT) campaign, approximately 670 days from explosion. This target was triggered based on the predicted gamma-ray luminosity (see Section 4.1 and Appendix for a description) derived from the optical observation. Although it was almost two years after the explosion, the nearby distance yielded a gamma-ray luminosity prediction still within reach of VERITAS, making this an enticing target to follow up.

The SN2017egm data in this paper were taken using “wobble” pointing mode, where the source is offset from the center of the camera by 0.5° . This mode creates space for a radially symmetric off region to be used for background estimation in the same field of view, saving time from targeted background observations that contain the same data observing conditions. The data were processed with standard VERITAS calibration and reconstruction pipelines, and then cross-checked with a separate analysis chain (Cogan 2008; Maier & Holder 2017).

Using an Image Template Method (ITM) to improve event angular and energy reconstruction (Christiansen 2017), analysis cuts are determined with a set of a priori data-selection cuts optimized on sources with a moderate power-law index (from -2.5 to -3).

Unfortunately, the large offset on SN2015bn due to the serendipitous observation precludes us from using ITM in the analysis, so in that case SN2015bn is analyzed without

³⁵ <https://fermipy.readthedocs.io/en/latest/>; v0.19.0.

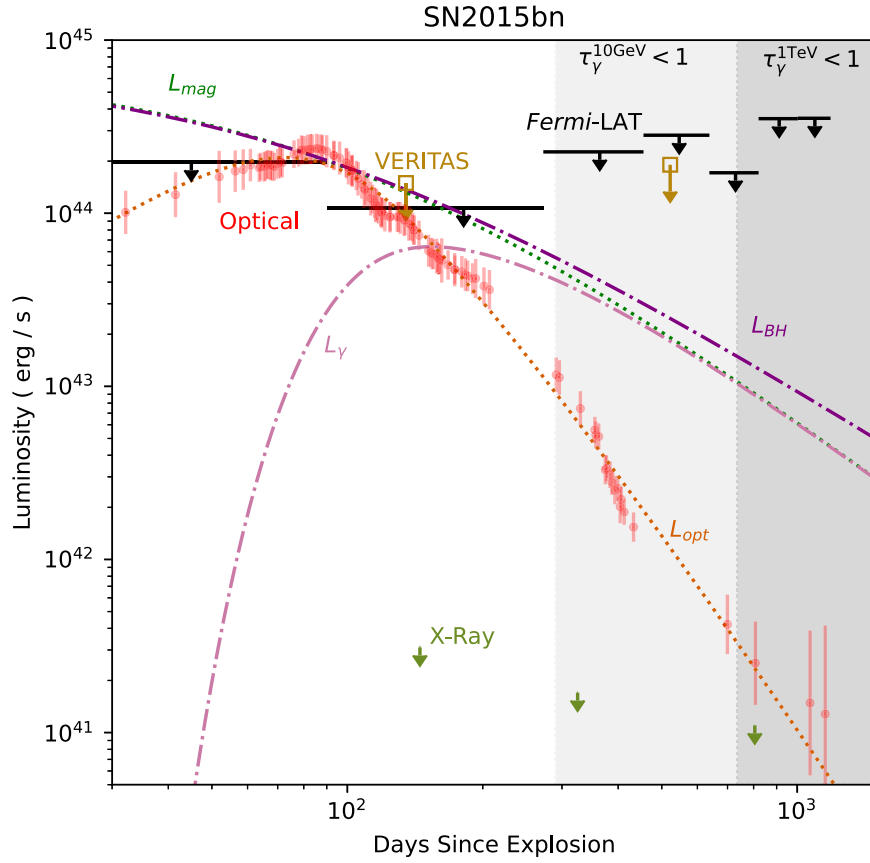


Figure 2. Light curves of SN2015bn spanning 30–1500 days after explosion. Curves shown include (1) the (thermal) supernova luminosity, L_{opt} , fit to UVOIR bolometric luminosity data (in red; Nicholl et al. 2018) to obtain the magnetar parameters; (2) magnetar spin-down luminosity, L_{mag} (green dotted lined); and (3) predicted gamma-ray luminosity that escape the ejecta, L_{γ} (pink dotted–dashed line; Equations (A.1), (A.3) and (A.4)). Black bars show Fermi-LAT upper limits reported for six 180 day bins starting ~ 90 days after explosion. The olive open box shows the VERITAS integral energy flux upper limit taken ~ 135 days after the explosion, with EBL absorption correction applied. Upper limits on the 0.2–10 keV X-ray luminosity from Chandra are from Bhimbhakdi et al. (2018) in green. Gray shaded regions labeled “ $\tau_{\gamma} < 1$ ” show the approximate time after which gamma-rays of the indicated energy should escape ejecta, based on Figure 1. A purple dotted–dashed line shows the engine luminosity, L_{BH} (Equation (1)), in an alternative model in which the supernova optical luminosity is powered by fallback accretion onto a black hole. All upper limits denote the 95% confidence level.

templates by calculating image moments directly from candidate images triggered by the camera (Cogan 2008; Maier & Holder 2017). In both cases, the signal and background counts are determined using the reflected region method.

The upper limit is calculated for both SN2015bn and SN2017egm. The bounded Rolke method for upper limit calculation is used, assuming a power-law spectrum with index of -2.0 and 95% confidence level (Rolke et al. 2005). Since the calculation of the upper limit depends on the underlying spectral model, a range of power-law spectral indices from -2 to -3 was computed to estimate impact of the model dependence. In all cases reported here, the upper limit reported is the integral photon flux, integrated over the energy ranges described for each case, which has units of $\text{cm}^{-2} \text{s}^{-1}$. This flux is converted to integral energy flux using the same spectral model so that the luminosity can be computed with the adopted distance.

3. Results

No statistically significant detections were made of either SN2015bn or SN2017egm across the energy range 100 MeV to 30 TeV. Integral energy upper limits are reported for the energy ranges given for each instrument. Figures 2 and 3 show the Fermi-LAT and VERITAS upper limits in comparison to the

supernova optical light curves and the theoretically predicted escaping luminosity from the magnetar model.

3.1. Optical

The SN2015bn integrated ultraviolet-optical-infrared (UVOIR) light-curve data are reproduced here from previous analyses (Nicholl et al. 2016a, 2016b, 2018). To produce these bolometric light curves, the multiband optical data were interpolated and integrated at each epoch using the code *superbol* (Nicholl 2018).

Similarly, the SN2017egm UVOIR data are also reproduced here with *superbol* (Bose et al. 2017; Nicholl et al. 2017a).

3.2. Fermi-LAT

Both SN2015bn and SN2017egm are not statistically significant sources in the first ~ 90 days or the subsequent 6 month bin starting 90 days after the explosion. These sources also remain undetected in any of the following 6 month bins, and in the multiyear data sets.

The evaluation of the integral energy flux upper limit for the Fermi-LAT observations within each time bin was performed assuming a power-law spectral model with an index of -2 . The model dependence of this calculation naturally impacts the interpretations in Section 4, so the fit was performed with

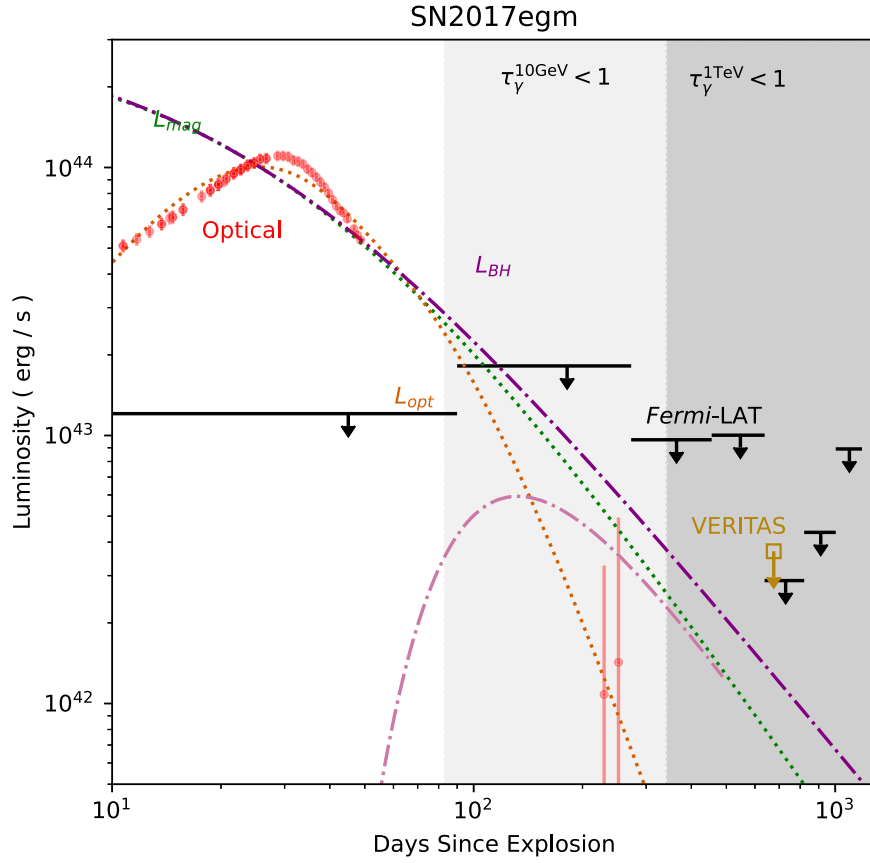


Figure 3. The SN2017egm light curve spanning 10–1300 days after explosion, following the same format as Figure 2. UVOIR data are shown in red (Bose et al. 2017; Nicholl et al. 2017a). Integral energy flux upper limits from Fermi-LAT are reported for six 180 day bins starting ~ 90 days after the explosion. Integral energy flux upper limits are shown for VERITAS data taken ~ 670 days after explosion, with EBL absorption correction applied. The maximum luminosity of the black hole accretion model L_{BH} (Equation (1)) is shown in purple. All upper limits denote the 95% confidence level.

indices 2, 2.5, and 3 to find the impact of the model on the final upper limit. An uncertainty of about 10% was found based on varying the index.

SN2015bn is found to have test statistic (TS) of 0.06, with 12 predicted events above the isotropic diffuse background $\simeq 4.8 \times 10^4$ events over the entire period. The flux upper limit is $1.6 \times 10^{-6} \text{ MeV cm}^{-2} \text{ s}^{-1}$ over the energy range 100 MeV to 500 GeV. In the first ~ 90 days after the explosion, where the gamma-ray emission is not expected due to the high gamma-ray absorption (see Figure 1), the flux upper limit is $3.5 \times 10^{-6} \text{ MeV cm}^{-2} \text{ s}^{-1}$ over the energy range 100 MeV to 500 GeV, with a TS of 0. For the first 6-month period, when the signal is most likely, the flux upper limit is $1.9 \times 10^{-6} \text{ MeV cm}^{-2} \text{ s}^{-1}$ for TS $\simeq 0$, consistent with a nondetection. All of the following 6 month bins reported nondetections with TS < 2 .

SN2017egm is found to have TS = 4.4, with 43 predicted events above the isotropic diffuse background $\simeq 5.9 \times 10^4$ events. The flux upper limit is $1.2 \times 10^{-6} \text{ MeV cm}^{-2} \text{ s}^{-1}$ over the energy range 100 MeV to 500 GeV. In the first ~ 90 days after the explosion, where the gamma-ray emission is not expected due to the high gamma-ray absorption (see Figure 1), the flux upper limit is $3.2 \times 10^{-6} \text{ MeV cm}^{-2} \text{ s}^{-1}$ over the energy range 100 MeV to 500 GeV, with a TS of 0. For the first 6 month period, when the signal is most likely, the flux upper limit is $4.9 \times 10^{-6} \text{ MeV cm}^{-2} \text{ s}^{-1}$ for TS = 10.1, consistent with a nondetection. All of the following 6 month bins reported nondetections with TS < 1 .

3.3. Veritas

Table 2 reports the results from VERITAS observations of SN2015bn and SN2017egm. Each observation is consistent with a nondetection. The significance of each excess of observed events above background is below 2 standard deviations (σ). The flux upper limits are also given, calculated by integrating above the threshold energy of the instrument.

The statistical significance of an excess is estimated using Equation (17) of Li & Ma (Li & Ma 1983). SN2015bn has significance value of -0.5σ in the first epoch observation. The integral flux upper limit from 0.32 to 30 TeV for SN2015bn is $2.85 \times 10^{-12} \text{ cm}^{-2} \text{ s}^{-1}$, which corresponds to an upper limit on the luminosity of $1.27 \times 10^{44} \text{ erg s}^{-1}$ at a redshift of 0.1136. Due to the serendipitous nature of the observation, SN2015bn is significantly off axis, which lowers the instrument sensitivity at the energy threshold of 320 GeV. Additionally, a 10% systematic uncertainty is added to the flux normalization and reported energy threshold due to instrument degradation during the period of 2012–2015 (Nievas Rosillo 2021). This uncertainty is derived empirically from the observation of the Crab Nebula over the same period. During the second observation in 2016, SN2015bn was found to have a significance of 1.7. The integral flux upper limit from 0.42 to 30 TeV for SN2015bn is $2.78 \times 10^{-12} \text{ cm}^{-2} \text{ s}^{-1}$, which corresponds to an upper limit on the luminosity of $1.60 \times 10^{44} \text{ erg s}^{-1}$.

For SN2017egm, the Li & Ma significance value is 0.2σ and an integral upper limit from 0.35 to 30 TeV is

Table 2
Results from VERITAS Observations for Both Epochs of SN2015bn and SN2017egm

Parameter	(Unit)	SN2015bn ₁	SN2015bn ₂	SN2017egm
Start (MJD)	[day]	57149	57533	58566
End (MJD)	[day]	57164	57538	58578
Live time	[hr]	1.0	1.8	8.7
On	[event]	4	10	49
Off	[event]	179	188	596
α^a	...	0.0286	0.0299	0.0634
Excess	[event]	−1.1	4.4	11.2
Significance	[σ]	−0.5	1.7	1.6
Flux UL	[$1 \times 10^{-13} \text{ cm}^{-2} \text{ s}^{-1}$]	28.5	27.8	10.2
$E_{\text{threshold}}$	[GeV]	>320	>420	>350

Notes. Shown are the quality selected live time, number of gamma-ray-like events in the on- and off-source regions, the normalization, the observed excess of the gamma-rays, and the statistical significance. The integral flux upper limit is shown for the given energy threshold, without EBL absorption correction, integrated up to 30 TeV.

^a Ratio of relative exposure for on and off regions.

$1.0238 \times 10^{-12} \text{ cm}^{-2} \text{ s}^{-1}$, which corresponds to an upper limit on the luminosity of $3.54 \times 10^{42} \text{ erg s}^{-1}$ above the energy threshold of 350 GeV at redshift $z=0.0310$. The systematic correction due to instrument degradation during the period of 2012–2019 is applied automatically with the use of the throughput-calibrated analysis templates (Nievas Rosillo 2021). In the cases of both SN2015bn and SN2017egm, the impact of varying the power-law model index parameter from -2 to -5 is about 10%, which is negligible in the context of their respective light curves.

VHE photons are absorbed by the extragalactic background light (EBL) throughout the universe, so the flux must be corrected to account for the missing photons. This absorption is energy and redshift dependent. Deabsorption is applied to the flux using the model of Domínguez et al. (2011). The EBL deabsorption factor was convolved with the upper limit calculation, assuming the same spectral shape (a power law with the photon index of -2.0). The deabsorbed integral photon upper limit for SN2015bn within the energy range 0.32–30 TeV, is $3.36 \times 10^{-12} \text{ cm}^{-2} \text{ s}^{-1}$, which corresponds to a luminosity upper limit of $1.49 \times 10^{44} \text{ erg s}^{-1}$. For the second observation, the deabsorbed integral photon upper limit for SN2015bn within the energy range 0.42–30 TeV, is $3.30 \times 10^{-12} \text{ cm}^{-2} \text{ s}^{-1}$, which corresponds to a luminosity upper limit of $1.91 \times 10^{44} \text{ erg s}^{-1}$. For SN2017egm, with a slightly smaller energy range 0.350–30 TeV, the deabsorbed integral photon flux is $1.07 \times 10^{-12} \text{ cm}^{-2} \text{ s}^{-1}$, which corresponds to a luminosity upper limit of $3.70 \times 10^{42} \text{ erg s}^{-1}$. These EBL-corrected values are plotted in Figure 2 and Figure 3.

4. Discussion

The source of the extra luminosity powering SLSNe-I may be found in the signature of its late-time gamma-ray emission. This section explores the HE to VHE emission hundreds of days after the explosion. The following models with a gamma-ray emission component for the powering mechanism are discussed: (1) magnetar central engine (see Section 4.1), (2) black hole central engine (see Section 4.2), and (3) circumstellar interaction (see Section 4.3).

4.1. Magnetar Central Engine

The most promising mechanism for powering SLSNe-I is the rotational energy input from a central magnetar. In this scenario, a young pulsar or magnetar inflates a nebula of relativistic particles, which radiate high-energy gamma-rays and X-rays. This section initially explores a simple implementation of the magnetar model (see Appendix for full description), followed by a more complete model described in detail in Vurm & Metzger (2021) for both SN2015bn and SN2017egm. The application of this so-called self-consistent model is necessary to directly predict the energy-dependent luminosities within the energy ranges of the Fermi-LAT and VERITAS observations, a major contribution that is not possible with simpler implementation described in the Appendix.

At early times after the explosion (around and immediately after the maximum in the optical emission) the gamma-rays are absorbed and thermalized by the expanding supernova ejecta. At these times, the luminosity and shape of the optical light curve can be used to constrain the parameters of the magnetar. In this model, the radiation of an input energy reservoir (the spin-down luminosity of a rotating magnetar) diffuses through the ejecta following the analytical solution by Arnett (1982) (Equation (A.3)).

The time evolution of the magnetar’s spin-down luminosity can be modeled by assuming a rotating dipole magnetic field whose energy loss is dominated by emission of radiation in the gamma-ray and X-ray bands (see Appendix for details).

This luminosity depends on the magnetar initial spin period, surface dipole magnetic field strength, and neutron star mass, $L_{\text{mag}}(t, P_0, B, M_{\text{NS}})$ (Equation (A.1)). The emitted radiation thermalizes as it diffuses through the ejecta. The conditions of the ejecta determine the optical and gamma-ray outputs, dominated by the values of the ejecta mass, ejecta velocity, and optical and gamma-ray opacities to form $L_{\text{opt}}(t, M_{\text{ej}}, v_{\text{ej}}, \kappa, \kappa_{\gamma})$ (Equation (A.4)) and $L_{\gamma}(t, M_{\text{ej}}, v_{\text{ej}}, \kappa, \kappa_{\gamma})$ (Equation (A.5)).

For SN2015bn and SN2017egm, the parameters for the magnetar and the supernova ejecta properties were found by fitting their integrated ultraviolet-optical-infrared (UVOIR) light curves, shown with red points in Figures 2 and 3. All fits were conducted using nonlinear least squares minimization.³⁶ The

³⁶ `scipy.optimize.curve_fit`.

best-fit parameters with errors for the magnetar model are given in Table 1. The redshifts and time of peak optical magnitude are shown in the table as listed in The Open Supernova Catalog (Guillochon et al. 2016).³⁷

These parameters are consistent with the results of previous fits (Nicholl et al. 2018, 2017a) that took into account both the optical spectral energy distribution and light curve using the open-source code MOSFIT.³⁸ The relative statistical errors on these fit parameters may be optimistic at $\sim 10\%$, and the systematic errors will still need to be incorporated for a better understanding the magnetar parameter space. The largest contributor to the magnetar power are the period and magnetic field values, which determine the overall magnitude of the luminosity. The ejecta mass and velocity determine the time to optical peak by the diffusion of the emission through the ejecta.

A particularly important shortfall of this model is the constant effective opacity to both optical and gamma-ray photons, rather than a time-dependent treatment of the opacity. TeV gamma-rays interact preferentially with optical photons, so at the time of the peak optical emission, $\gamma\gamma$ absorption by optical photons will be high, reducing any predicted gamma-ray emission by this model. Equation (A.4) is a bolometric luminosity, so it does not take into account the energy and time-dependent opacity, instead fitting a constant effective κ and κ_γ to generate the time-dependent optical depth.

Therefore, Figure 1 is used as a guide for when to expect L_γ to provide an appropriate estimate for the gamma-ray emission. The shaded regions in Figures 2 and 3 estimate the time periods when photons of the given energies can escape. It is important to reiterate that this model is energy independent, representing the bolometric luminosity not thermalized by the ejecta. This model cannot distinguish the emission between LAT and VERITAS energy bands since it does not consider the physical model of the nebula; the self-consistent model described by Vurm & Metzger (2021) and discussed below will be an attempt to do so explicitly.

Following the methodology in the Appendix with the magnetar parameters for each SLSN, $L_{\text{mag}}(t)$, $L_{\text{opt}}(t)$, and $L_\gamma(t)$ were calculated and are shown in comparison to the gamma-ray limits in Figures 2 and 3.

For SN2015bn (Figure 2), neither the Fermi-LAT upper limits nor the VERITAS upper limit constrain the predicted escaping luminosity. Similarly, for SN2017egm (Figure 3), both the VERITAS and Fermi-LAT upper limits are not deep enough to constrain the predicted escaping luminosity. An important caveat to these upper limits is that the escaping luminosity may also be emitted at energies not explored here, such as hard X-rays or gamma-rays greater than 30 TeV.

The optimal time to observe with a pointed instrument sensitive at a particular photon energy results from a trade-off between the dropping ($\propto t^{-2}$) magnetar luminosity and the rising transparency of the ejecta; predicting the optimal time post-peak to observe requires knowledge of the evolution of the optical spectrum. It is possible to accumulate enough optical data within a few weeks after the optical peak to fit the magnetar model for a reliable prediction of the gamma-ray luminosity. In the case of SN2017egm, the gamma-ray luminosity prediction was anchored by the late optical data points about 1 yr after the explosion. This means that had the VERITAS observations been taken at that point (more than a

year earlier than the original observation), they would have been deeply constraining to the magnetar model.

Going beyond these relatively model-independent statements to compare to a more specific spectral energy distribution for the escaping magnetar nebula requires a detailed model for the nebula emission and its transport through the expanding supernova ejecta. Such a model offers preliminary support that a significant fraction of L_γ may come out in the VHE band (Vurm & Metzger 2021). In this case, the VHE limits on SN2015bn and SN2017egm do not strongly constrain the parameters of the magnetar model, such as the nebular magnetization.

The model of Vurm & Metzger (2021) self-consistently follows the evolution of high-energy electron/positron pairs injected into the nebula by the magnetar wind and their interaction with the broadband radiation and magnetic fields. They found that the thermalization efficiency and the amount of gamma-ray leakage depends strongly on the nebular magnetization, ε_B , i.e., the fraction of residual magnetic energy in the nebula relative to that injected by the magnetar.

The model is simulated for dimensionless ε_B values set between 10^{-6} and 10^{-2} ; the higher magnetizations lead to greater synchrotron efficiencies, which dominate within a few hundred days, and lead to the optical emission tracking the spin-down luminosity. Lowering the magnetization to 10^{-7} – 10^{-6} for SLSN-I events like those in this work delays the transition to synchrotron-dominated thermalization, so that the predicted optical emission actually tracks the observed data.

The theoretical light curves and gamma-ray upper limits are shown in Figure 4. Vurm & Metzger (2021) concluded that the predicted low magnetizations constrained by the optical data alone presents new challenges to the theoretical framework regarding the dissipation of the nebular magnetic field. This may invoke magnetic reconnection ahead of the wind-termination shock or near the termination shock through forced reconnection of alternating field stripes described in Komissarov (2013), Lyubarsky (2003), and Margalit et al. (2018b). It is also possible that the true luminosity of the central engine decreases faster in time than the simpler $\propto t^{-2}$ magnetic spin down, such that escaping VHE emission is not necessary to explain the model. These VHE upper limits do not rule out this model, and do not settle the challenges inferred by the low magnetization required to fit the optical data. Further observations are needed to probe the nebular magnetization and synchrotron efficiency, and deep VHE observations will contribute to these constraints.

The nondetection of X-rays for both events is consistent with the predictions of Margalit et al. (2018a) of a fully ionized ejecta. Even under the most optimistic conditions—an engine that puts 100% of its spin-down luminosity into ionizing photons of ideal energies—cannot reduce the opacity enough to allow X-rays to escape under the usual assumptions (e.g., spherically symmetric ejecta shell).

4.2. Black Hole Central Engine

Instead of forming a neutron star like a magnetar, a SLSN-I might form a black hole, in which case the optical peak of the light curve could be powered by energy released from the fallback accretion of ejecta from the explosion (e.g., Dexter & Kasen 2013). Even if a black hole does not form immediately, it could form at late times once the magnetar accretes enough fallback material (Moriya et al. 2016). The main practical difference as compared to a magnetar in Section 4.1 is that the black hole central-engine power would be predicted to decay

³⁷ <https://sne.space>

³⁸ <https://mosfit.readthedocs.io/en/latest/>

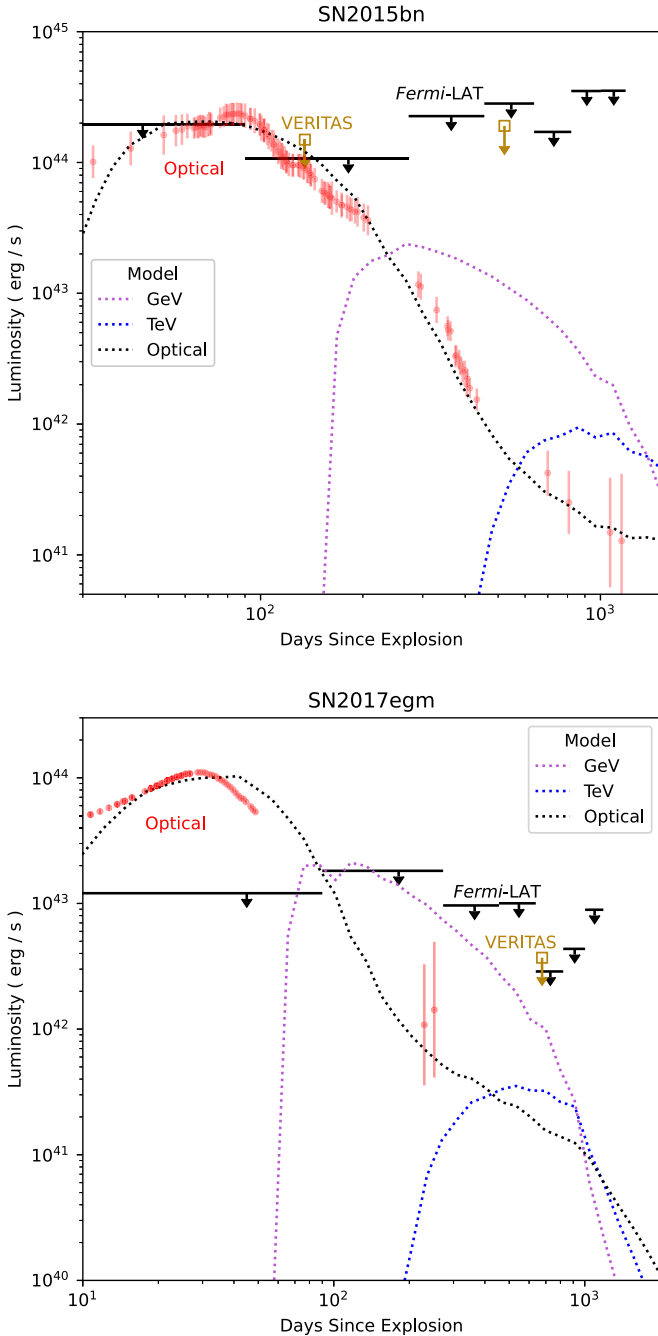


Figure 4. Model light curve for nebular magnetization (from Vurm & Metzger 2021) for SN2015bn with $\varepsilon_B = 10^{-7}$ (top panel) and SN2017egm with $\varepsilon_B = 10^{-6}$ (bottom panel).

with the fallback accretion rate $\dot{M}_{fb} \propto t^{-5/3}$ instead of $\propto t^{-2}$. Thus, in principle, for the same luminosity at the time of the optical maximum t_{pk} , the central-engine output at times $t \gg t_{pk}$ could be enhanced by a factor $\propto (t/t_{pk})^{1/3} \sim 2$ for $t \sim 1$ yr and $t_{pk} \sim 1$ month, thus tightening our constraints.

In Figures 2 and 3, a rough estimate of the maximal engine luminosity in the BH accretion scenario is shown, which is calculated as

$$L_{BH} = \frac{2^{5/3} L_{opt}^{pk}}{\left(1 + \frac{t}{t_{pk}}\right)^{5/3}}, \quad (1)$$

where L_{opt}^{pk} is the peak optical luminosity, scaled so that $L_{BH} = L_{opt}$ around the optical peak.

On the other hand, while gamma-rays are naturally expected from the ultra-relativistic spin-down-powered nebula of a magnetar, it is less clear that this would be the case for a black hole engine. For instance, the majority of the power from a black hole engine could emerge in a mildly relativistic wind from the black hole accretion disk instead of an ultra-relativistic spin-down-powered pulsar wind.

As seen in both Figure 2 (SN2015bn) and Figure 3 (SN2017egm), the gamma-ray emission in the black hole scenario is not constrained in the Fermi-LAT and VERITAS energy bands.

4.3. Circumstellar Interaction

An alternative model for powering the light curve of SLSNe is to invoke the collision of the supernova ejecta with a slower expanding circumstellar shell or disk surrounding the progenitor at the time of the explosion (e.g., Smith & Owocki 2006; Chevalier & Irwin 2011; Moriya et al. 2013). Features of this circumstellar model (CSM), such as the narrow hydrogen emission lines that indicate the interaction of a slow-moving gas, provide compelling evidence for this being a powering mechanism for many but not all of the hydrogen-rich class of SLSNe (SLSNe-II; e.g., Smith et al. 2007; Nicholl et al. 2020).

Shock interaction could in principle also power some hydrogen-poor SLSNe (SLSNe-I), particularly in cases where the circumstellar interaction is more deeply embedded and less directly visible (e.g., Sorokina et al. 2016; Kozyreva et al. 2017). There is growing evidence for hydrogen-poor supernovae showing hydrogen features from the interaction in their late-time spectra (Milisavljevic et al. 2015; Yan et al. 2015, 2017; Chen et al. 2018; Kuncarayakti et al. 2018; Mauerhan et al. 2018). The light echo from iPTF16eh (Lunnan et al. 2018) implies a significant amount of hydrogen-poor circumstellar medium in a SLSN-I at $\sim 10^{17}$ cm. However, this material is too distant for the ejecta to reach by the time of maximum optical light and hence cannot be responsible for boosting the peak luminosity.

In principle, the gamma-ray observations of SLSNe can constrain shock models. In many cases, this may not work out since most of the emission from shock-heated plasma is expected to either (1) come out in the X-ray band, as is well studied in other CSM-powered supernovae such as SNe IIn like SN 1998S (Pooley et al. 2002), SN 2006jd (Chandra et al. 2012), SN 2010jl (Chandra et al. 2015), and SNe Ib/c (Chevalier & Fransson 2006), or (2) be absorbed by the surrounding ejecta and reprocessed into the optical band. Thus, these VHE limits on SLSNe do not constrain the bulk of the shock power.

Higher-energy radiation can be produced if the shocks accelerate a population of nonthermal relativistic particles that interact with ambient ions or the supernova optical emission to generate gamma-rays (e.g., via the decay of π^0 generated via hadronic interactions with matter and radiation; e.g., Murase et al. 2011). However, because shocks typically place a fraction $\epsilon_{rel} \lesssim 0.1$ of their total power into relativistic particles (or even less; Steinberg & Metzger 2018; Fang et al. 2019), the predicted gamma-ray luminosities (matching the same level of optical emission as magnetar models) would be at least 10 times lower than L_γ predicted by the magnetar nebula scenario, thus rendering our VHE upper limits unconstraining on

nonthermal emission from shocks on SN2015bn and SN2017egm. This is consistent with upper limits from the Type IIIn SN 2010j from Fermi-LAT, which Murase et al. (2019) used to constrain $\epsilon_{\text{rel}} \lesssim 0.05 - 0.1$.

5. Future Prospects

These results demonstrate that high-energy gamma-ray observations of SLSN-I are on the brink of enabling constraints on the light curves and even spectral energy distribution of magnetar models. Given the rarity of bright, nearby SLSN-I, and the need to take observations in the optimal window (when L_γ is near maximum), careful planning will be required to make progress going ahead (Quimby et al. 2011; McCrum et al. 2015; Prajs et al. 2017). The strategy outlined below will focus only on SLSN-I, as type II SLSN are likely to be powered by a mechanism that requires a different consideration of the temporal and spectral evolution of the gamma-ray emission.

Standard arrays of IACTs provide an improved instantaneous sensitivity to gamma-ray emission over Fermi-LAT due to 10^4 – 10^5 larger effective area, counterbalanced in part by the pointed nature of their observations. To propose a strategy, we first revisited the characteristics of a large sample of observed SLSNe and performed a systematic study.

Nicholl et al. (2017b) fit a sample of 38 SLSNe light curves using MOSFiT to obtain a distribution of magnetar model parameters. This sample is a selection of SLSNe with well-observed events classified as Type I with published data near the optical peak, forming a representative sample of good SLSNe-I for a population study. For each event in this sample, the following was calculated: the escaping gamma-ray luminosity L_γ following the procedure outlined in Appendix and the flux $F_\gamma = L_\gamma / 4\pi D_L^2$ based on the source luminosity distance D_L . In performing this analysis, rather than fitting the value of κ_γ individually to each optical light curve (as done in Nicholl et al. 2017b), the value $\kappa_\gamma = 0.01 \text{ cm}^2 \text{ g}^{-1}$ is fixed in all events, based on the best-fit to SN2015bn (given its particularly high-quality late-time data, which provides the most leverage on κ_γ).

The results for $F_\gamma(t)$ are shown in the top panel of Figure 5. In the magnetar model, the predicted gamma-ray flux could emerge anywhere across the HE to VHE bands; hence, it represents an upper limit on flux in the bands accessible to Fermi-LAT and IACTs. The bottom two panels of Figure 5 show the distribution of the peak escaping flux $F_{\gamma, \text{max}}$ and time of the peak flux relative to the explosion. For most SLSNe-I presented here, $F_{\gamma, \text{max}}$ is well below the sensitivity of VERITAS and even the future Cherenkov Telescope Array (CTA) (The CTA Consortium 2019). Also note that the characteristic timescale to achieve the peak gamma-ray flux is ≈ 2 –3 months from the explosion. This timescale occurs approximately at the same time as when the optical depth of the ejecta to VHE emission falls below unity, when the VHE photons can escape (Figure 1).

Figure 6 shows $F_{\gamma, 600\text{d}}$ as a function of the peak optical magnitude of the SLSNe-I from the same sample as in Figure 5. The selection of fluxes at 600 days approximates the time when the effective opacity to 1 TeV photons reaches 1, based on Figure 1. The top axis also gives the all-sky rate of SLSNe-I above a given peak optical magnitude, which is estimated using the magnitude distribution of SLSNe-I and assuming they occur at a comoving volumetric rate of $R(z) = 19(1+z)^{3.28} \text{ Gpc}^{-3} \text{ yr}^{-1}$ following Nicholl et al. (2017c), Lunnan et al. (2018),

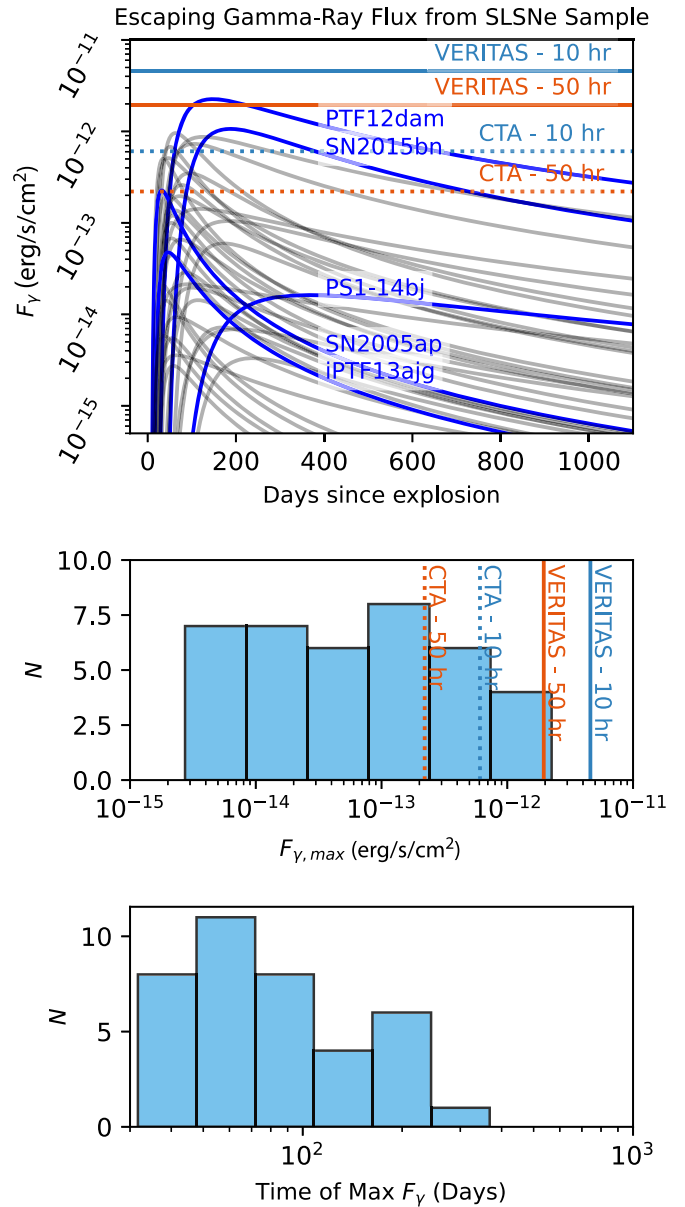


Figure 5. Top: escaping gamma-ray luminosity $L_\gamma(t)$ for the sample of SLSNe fit by Nicholl et al. (2017b). Five well-studied SN are highlighted in blue, including SN2015bn. Overplotted are the VERITAS and CTA sensitivity curves for various exposures. Middle: distribution of peak escaping gamma-ray flux $F_{\gamma, \text{max}} = \max[L_\gamma]/4\pi D^2$, for the light curves from the top panel where D is the distance to each source. Again, VERITAS and CTA sensitivities for different exposures are shown as vertical dashed lines. Bottom: distributions of times since explosion to reach the maximum gamma-ray flux $F_{\gamma, \text{max}}$ from F_γ above.

De Cia et al. (2018). This estimation captures the general volumetric rate of events, but is unreliable for exceptionally bright events such as SN2017egm due to the small population for estimating the magnitude normalization. A bright event like SN2017egm may actually happen more often than once a century.

Shown for comparison in Figure 6 are the integral sensitivities of various gamma-ray instruments for different exposures. For IACT instruments such as VERITAS and the future CTA, sensitivity is defined as the minimum flux necessary to reach 5σ detection of a point-like source, requiring at least 10 excess gamma-rays and the number of signal counts at least 5% of the number of background counts. For

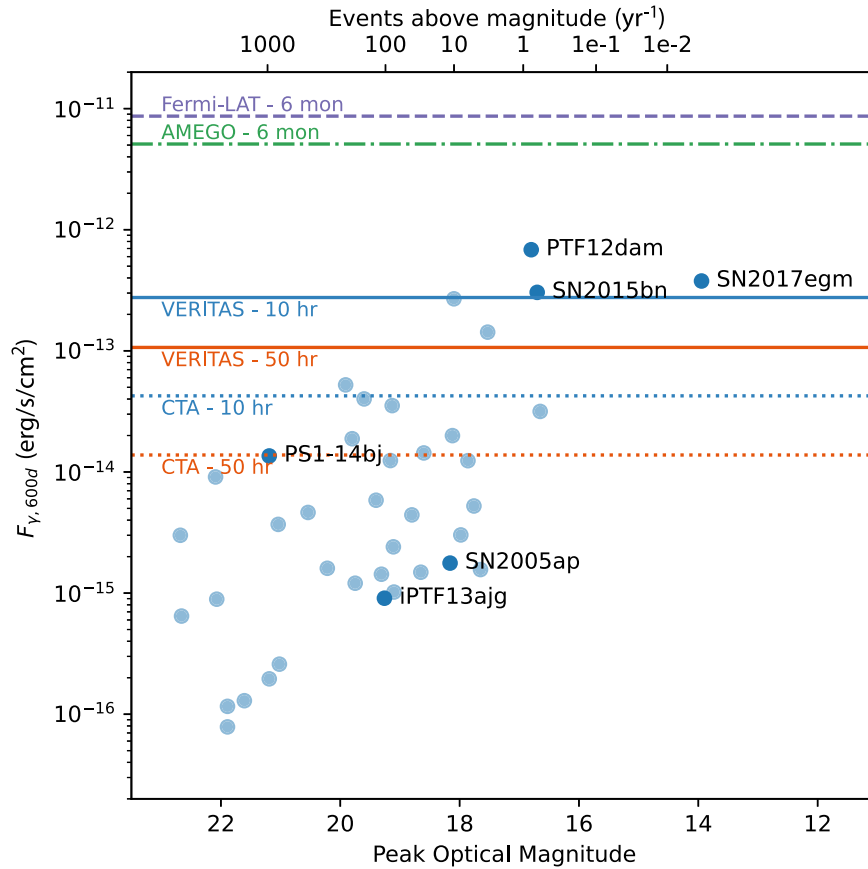


Figure 6. Blue dots show the peak optical apparent magnitudes of a sample of SLSNe-I (Nicholl et al. 2017b) as a function of their predicted maximum gamma-ray luminosity at 600 days after explosion ($F_{\gamma,600d}$). The top axis shows the approximate rate of events above the given peak optical magnitude, calculated using the method described in the main text. Peak maximum gamma-ray luminosities are calculated from fits of optical data with fixed $\kappa_{\gamma} = 0.01 \text{ cm}^2 \text{ g}^{-1}$. Integral sensitivities of various instruments are overplotted for different exposures. Solid lines: VERITAS 10 and 50 hr integral sensitivities above 220 GeV. Dotted lines: CTA (in development) 10 and 50 hr integral sensitivities above 125 GeV as estimated from 50 hr Monte Carlo simulations of the southern array (The CTA Consortium 2019) and extrapolated to 10 hr. Similar extrapolation is done for Fermi-LAT from 10 yr to 6 months (Nolan et al. 2012) (dashed line). Proposed project AMEGO integral sensitivity above 100 MeV for 6 month observation window is also plotted (dashed-dotted line) (Kierans et al. 2020).

VERITAS, the sensitivity was calculated using observed Crab Nebula data to estimate the rates of signal and background photons with cuts optimized for a $\Gamma = -2.5$ power-law spectrum, and then rescaled for the appropriate observation time (Park 2015). For CTA, Monte Carlo simulations were used to derive angular resolution, background rates and energy dispersion features—the instrument response functions (IRF)—based on the Prod3b-v2 telescope configuration for the Southern site and its atmosphere (Observatory 2016). These IRFs are publicly available and were analyzed using the open-source CTOOLS³⁹ (Knödseder et al. 2016a). A power-law spectral model was used to estimate the integral sensitivity above 0.125 and 1 TeV each for observations of 10 and 50 hr (see Fioretti et al. 2016 for further discussion on CTA integral sensitivity).

Based on this systematic study, we propose the following observation strategy: (1) Receive automated public alert and Type I classification of SLSN from a survey instrument such as the Zwicky Transient Facility (ZTF). Classification is generally determined by identification of early spectral components such as O II absorption features. (2) During the multiday rise and fall of bolometric optical light curve, fit the magnetar model (L_{opt} , yielding parameters for L_{mag} and L_{γ}). (3) Compare L_{γ} to the

telescope sensitivity at the appropriate day when the effective $\gamma\text{-}\gamma$ opacity falls below ~ 1 for the telescope’s sensitive energy range (see Figure 1). In the case of IACTs sensitive to energies above 100 GeV, the gamma-rays will escape the magnetar a few hundred days after explosion, requiring a bright SLSN-I that will power gamma-rays for as much as two years.

Estimating $\sim 35\%$ of all-sky visibility at VERITAS due to Sun, Moon, and seasonal weather cut, and above 60° elevation, VERITAS is capable of detecting up to ~ 0.4 and ~ 4 SLSNe-I per year for 10 hr and 50 hr exposures, respectively. The next-generation CTA observatory will be able to detect as many as ~ 8 and ~ 80 events for 10 hr and 50 hr, respectively, assuming a larger sky visibility fraction of $\sim 80\%$ when both North and South arrays are included. On the other hand, SLSNe at greater distances also imply a stronger role of $\gamma\text{-}\gamma$ interactions on the EBL in suppressing the $\gtrsim \text{TeV}$ emission, decreasing the observed integral flux by as much as 60 times at redshifts near 0.5 in the VERITAS energy range.

Figure 7 shows the distribution of fluxes at 200 days and 600 days which are approximate average dates when the opacity to 100 GeV and 1 TeV photons falls below 1, respectively, and they are able to escape the ejecta. Accounting for this time delay for the opacity to drop, the expected rate of bright events drops by another 3–15 times. While past observations have not been followed up until this publication, the distribution of predicted gamma-ray fluxes hints that,

³⁹ <http://cta.irap.omp.eu/ctools/>

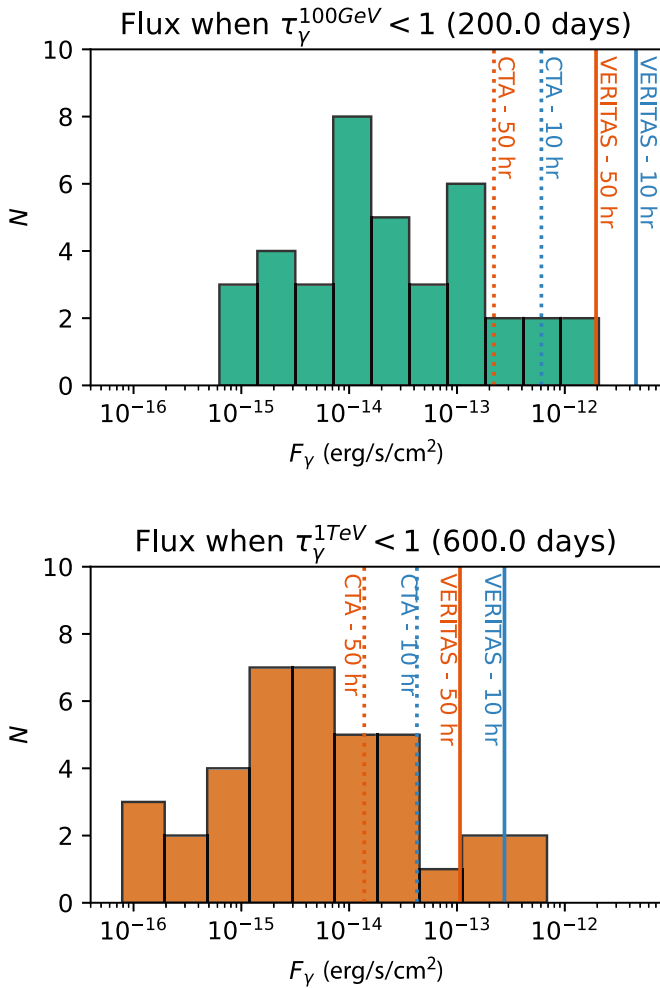


Figure 7. Distribution of gamma-ray luminosities L_γ at $t = 200$ days (top) and $t = 600$ days (bottom), when the optical depth for 100 GeV and 1 TeV photons drops below 1, calculated for a sample of 38 SLSNe (Nicholl et al. 2017b).

particularly for 100 GeV photons, future SLSN-I will be observable with current and planned observatories.

6. Conclusion

SLSN-I are potential gamma-ray emitters, and this paper provides the first upper limits at different times after the optical outburst for two good candidates. The reported upper limits approach the magnetar spin-down luminosity limit of SN2015bn and SN2017egm. While the expected gamma-ray luminosity in either the magnetar central-engine scenario or the shock-acceleration scenario is not constrained by these limits, a relativistic jet powered by fallback accretion onto a black hole is disfavored in both cases. We explore prospects for obtaining improved VHE gamma-ray constraints in the future by current and planned IACTs. We estimate the Type I SLSNe rate for VERITAS and CTA, considering observation constraints and the time delay due to the optical depth. For sufficiently nearby and bright SLSN-I, 0.4 and 4 events per year can be observed by VERITAS from 10 and 50 hr observation, respectively, and similarly rates of 8 and 80 events per year can be expected by CTA.

This research is supported by grants from the U.S. National Science Foundation and the Smithsonian Institution, by

NSERC in Canada, and by the Helmholtz Association in Germany. M.N. is supported by the European Research Council (ERC) under the European Unions Horizon 2020 research and innovation program (grant agreement No. 948381) and by a Fellowship from the Alan Turing Institute. I.V. acknowledges support by the ETAG grant PRG1006 and by EU through the ERDF CoE grant TK133. V.V.D.’s work is supported by NSF grant 1911061 awarded to the University of Chicago (PI: Vikram Dwarkadas). We acknowledge the excellent work of the technical support staff at the Fred Lawrence Whipple Observatory and at the collaborating institutions in the construction and operation of the instrument. This research has made use of the CTA instrument response functions provided by the CTA Consortium and Observatory, see <http://www.cta-observatory.org/science/cta-performance/> (version prod3b-v2) for more details.

Facilities: VERITAS, Fermi-LAT.

Software: fermipy (v0.19), (Wood et al. 2017), astropy (Robitaille et al. 2013; Price-Whelan et al. 2018), CTOOLS, (Knödlseder et al. 2016b), superbol (Nicholl 2018), EventDisplay (Maier & Holder 2017), VEGAS (Cogan 2008).

Appendix Magnetar Light Curve Model

Following Woosley (2010) and Kasen & Bildsten (2010), the spin-down power of a strongly magnetized, young neutron star (“magnetar”) at a time t after its birth is given by the magnetic dipole luminosity,

$$L_{\text{mag}}(t) = \frac{E_{\text{rot}}}{\tau_p} \frac{2}{(1 + 2t/\tau_p)^2}. \quad (\text{A1})$$

Here, $E_{\text{rot}} = (1/2)I_{\text{NS}}\Omega_i^2 \approx 2.6 \times 10^{52}(M_{\text{NS}}/1.4M_\odot)^3 P^{-2}$ erg is the magnetar rotational energy, I_{NS} is its moment of inertia, and M_{NS} is the neutron star mass. The spin-down time is given by $\tau_p = (6I_{\text{NS}}c^3/B^2R_{\text{NS}}^6\Omega_i^2) \approx 1.3 \times 10^5 B_{14}^{-2} P^2 (M_{\text{NS}}/1.4M_\odot)^{3/2} \sin^{-2}(\theta_B = 90^\circ)$ s, where $B = 10^{14} B_{14}$ G is the dipole magnetic field strength, P (ms) is the birth spin period ($\Omega = 2\pi/P$ is the birth angular velocity), and θ_B is the inclination angle of the magnetic dipole axis relative to the rotation axis.

Magnetar energy deposited behind the ejecta shell is assumed to thermalize and then diffuse outward through the ejecta as electromagnetic radiation. This occurs over a characteristic diffusion time (Arnett 1982)

$$\tau_m = \left(\frac{2\kappa M_{\text{ej}}}{\beta c v} \right)^{1/2}, \quad (\text{A2})$$

where M_{ej} , v , and κ are the total mass, mean velocity, and (optical wavelength) opacity of the supernova ejecta, respectively, and $\beta \approx 13.7$ is a constant. In most cases, τ_m sets the peak timescale of the supernova light curve.

To allow for the possibility that high-energy photons from the central magnetar nebula can escape instead of thermalizing, one can apply a trapping coefficient $(1 - e^{-\tau_\gamma})$ where the optical depth of the ejecta to gamma-rays can be written as $\tau_\gamma = At^{-2}$, where $A \equiv (3\kappa_\gamma M_{\text{ej}}/4\pi v_{\text{ej}}^2)$ and κ_γ is an effective gamma-ray opacity (Clocchiatti & Wheeler 1997; Chatzopoulos et al. 2012). For large $\tau_\gamma \gg 1$ (early times), the effects of gamma-ray leakage are small and the optical light curve (after the optical peak, at times $\gtrsim \tau_m$) will follow the spin-down luminosity, i.e., $L_{\text{opt}} \approx L_{\text{mag}}$. However, at late times when $\tau_\gamma \ll 1$, one has

$L_{\text{opt}} \ll L_{\text{mag}}$, with the remaining luminosity $L_{\gamma} = L_{\text{tot}} - L_{\text{opt}}$ escaping as gamma-rays.

More precisely, the luminosity of the magnetar (Equation (A.1)) that escapes the ejecta via photon diffusion by time t is calculated by Arnett (1982); Inserra et al. (2013)

$$L_{\text{tot}}(t) = \frac{2}{\tau_m} e^{-(\frac{t}{\tau_m})^2} \times \int_0^t dt' L_{\text{mag}}(t') e^{(\frac{t'}{\tau_m})^2} \frac{t'}{\tau_m} \quad (\text{A3})$$

Of this total luminosity, only a fraction is able to thermalize and hence power the optical supernova light curve,



$$L_{\text{opt}}(t) = (1 - e^{-A t^{-2}}) L_{\text{tot}}(t), \quad (\text{A4})$$

with the remainder instead escaping as gamma-rays,

$$L_{\gamma} = L_{\text{tot}} - L_{\text{opt}} = e^{-A t^{-2}} \frac{2E_p}{\tau_p \tau_m} e^{-(\frac{t}{\tau_m})^2} \int_0^t dt' \frac{2}{(1 + 2t'/\tau_p)^2} e^{(\frac{t'}{\tau_m})^2} t' \quad (\text{A5})$$

ORCID iDs

A. Acharyya  <https://orcid.org/0000-0002-2028-9230>
 C. B. Adams  <https://orcid.org/0000-0002-9021-6192>
 P. Bangale  <https://orcid.org/0000-0002-3886-3739>
 W. Benbow  <https://orcid.org/0000-0003-2098-170X>
 J. H. Buckley  <https://orcid.org/0000-0001-6391-9661>
 M. Capasso  <https://orcid.org/0000-0002-8136-9461>
 V. V. Dwarkadas  <https://orcid.org/0000-0002-4661-7001>
 M. Errando  <https://orcid.org/0000-0002-1853-863X>
 A. Falcone  <https://orcid.org/0000-0002-5068-7344>
 Q. Feng  <https://orcid.org/0000-0001-6674-4238>
 J. P. Finley  <https://orcid.org/0000-0002-8925-1046>
 G. M. Foote  <https://orcid.org/0000-0002-2944-6060>
 L. Fortson  <https://orcid.org/0000-0002-1067-8558>
 A. Furniss  <https://orcid.org/0000-0003-1614-1273>
 A. Gent  <https://orcid.org/0000-0001-7429-3828>
 W. F. Hanlon  <https://orcid.org/0000-0002-0109-4737>
 O. Hervet  <https://orcid.org/0000-0003-3878-1677>
 T. B. Humensky  <https://orcid.org/0000-0002-1432-7771>
 W. Jin  <https://orcid.org/0000-0002-1089-1754>
 P. Kaaret  <https://orcid.org/0000-0002-3638-0637>
 M. Kherlakian  <https://orcid.org/0000-0003-4686-0922>
 D. Kieda  <https://orcid.org/0000-0003-4785-0101>
 T. K. Kleiner  <https://orcid.org/0000-0002-4260-9186>
 S. Kumar  <https://orcid.org/0000-0002-5167-1221>
 M. J. Lang  <https://orcid.org/0000-0003-4641-4201>
 M. Lundy  <https://orcid.org/0000-0003-3802-1619>
 G. Maier  <https://orcid.org/0000-0001-9868-4700>
 C. E. McGrath  <https://orcid.org/0000-0001-5544-1434>
 J. Millis  <https://orcid.org/0000-0002-2069-9838>
 P. Moriarty  <https://orcid.org/0000-0002-1499-2667>
 R. Mukherjee  <https://orcid.org/0000-0002-3223-0754>
 M. Nievas-Rosillo  <https://orcid.org/0000-0002-8321-9168>
 S. O'Brien  <https://orcid.org/0000-0002-9296-2981>
 R. A. Ong  <https://orcid.org/0000-0002-4837-5253>
 S. R. Patel  <https://orcid.org/0000-0001-8965-7292>
 K. Pfrang  <https://orcid.org/0000-0002-7990-7179>
 M. Pohl  <https://orcid.org/0000-0001-7861-1707>
 E. Pueschel  <https://orcid.org/0000-0002-0529-1973>
 J. Quinn  <https://orcid.org/0000-0002-4855-2694>
 K. Ragan  <https://orcid.org/0000-0002-5351-3323>

D. Ribeiro  <https://orcid.org/0000-0002-7523-7366>
 J. L. Ryan  <https://orcid.org/0000-0001-6662-5925>
 I. Sadeh  <https://orcid.org/0000-0003-1387-8915>
 M. Santander  <https://orcid.org/0000-0001-7297-8217>
 G. H. Sembroski  <https://orcid.org/0000-0003-1329-3909>
 R. Shang  <https://orcid.org/0000-0002-9856-989X>
 M. Splettstoesser  <https://orcid.org/0000-0003-3407-9936>
 D. Tak  <https://orcid.org/0000-0002-9852-2469>
 A. Weinstein  <https://orcid.org/0000-0002-2126-2419>
 D. A. Williams  <https://orcid.org/0000-0003-2740-9714>
 B. D. Metzger  <https://orcid.org/0000-0002-4670-7509>
 M. Nicholl  <https://orcid.org/0000-0002-2555-3192>
 I. Vurm  <https://orcid.org/0000-0003-1336-4746>

References

- Abdalla, H., Aharonian, F., Ait Benkhali, F., et al. 2019, *A&A*, **626**, A57
 Abdollahi, S., Acero, F., Ackermann, M., et al. 2020, *ApJS*, **247**, 33
 Ahnen, M. L., Ansoldi, S., Antonelli, L. A., et al. 2017, *A&A*, **602**, A98
 Arnett, W. D. 1982, *ApJ*, **253**, 785
 Atwood, W. B., Abdo, A. A., Ackermann, M., et al. 2009, *ApJ*, **697**, 1071
 Bhrombhakdi, K., Chornock, R., Margutti, R., et al. 2018, *ApJL*, **868**, L32
 Bose, S., Dong, S., Pastorello, A., et al. 2017, *ApJ*, **853**, 57
 Chandra, P., Chevalier, R. A., Chugai, N., et al. 2012, *ApJ*, **755**, 110
 Chandra, P., Chevalier, R. A., Chugai, N., Fransson, C., & Soderberg, A. M. 2015, *ApJ*, **810**, 32
 Chatzopoulos, E., Craig Wheeler, J., & Vinko, J. 2012, *ApJ*, **746**, 121
 Chen, T. W., Smartt, S. J., Jerkstrand, A., et al. 2015, *MNRAS*, **452**, 1567
 Chen, X., Kou, S., & Liu, X. 2018, *ApJ*, **890**, 177
 Chevalier, R. A., & Fransson, C. 2006, *ApJ*, **651**, 381
 Chevalier, R. A., & Irwin, C. M. 2011, *ApJL*, **729**, L6
 Christiansen, J. 2017, *Proc. ICRC (Busan)*, **301**, 789
 Clocchiatti, A., & Wheeler, J. C. 1997, *ApJ*, **491**, 375
 Cogan, P. 2008, *Proc. ICRC (Yucatán)*, **3**, 1385
 De Cia, A., Gal-Yam, A., Rubin, A., et al. 2018, *ApJ*, **860**, 100
 Dessart, L., Hillier, D. J., Waldman, R., Livne, E., & Blondin, S. 2012, *MNRAS*, **426**, L76
 Dexter, J., & Kasen, D. 2013, *ApJ*, **772**, 30
 Domínguez, A., Primack, J. R., Rosario, D. J., et al. 2011, *MNRAS*, **410**, 2556
 Eftekhari, T., Berger, E., Margalit, B., et al. 2019, *ApJL*, **876**, L10
 Fang, K., Metzger, B. D., Murase, K., Bartos, I., & Kotera, K. 2019, *ApJ*, **878**, 34
 Fioretti, V., Bulgarelli, A., Schüssler, F., et al. 2016, *Proc. SPIE*, **9906**, 990630
 Gal-Yam, A. 2019, *ARA&A*, **57**, 305
 Guillochon, J., Parrent, J., Kelley, L. Z., & Margutti, R. 2016, *ApJ*, **835**, 64
 Holder, J., Atkins, R. W., Badran, H. M., et al. 2006, *APh*, **25**, 391
 Howell, D. A., Kasen, D., Lidman, C., et al. 2013, *ApJ*, **779**, 98
 Inserra, C., Smartt, S. J., Jerkstrand, A., et al. 2013, *ApJ*, **770**, 128
 Jerkstrand, A., Smartt, S. J., Inserra, C., et al. 2017, *ApJ*, **835**, 13
 Kasen, D., & Bildsten, L. 2010, *ApJ*, **717**, 245
 Kierans, C. A. 2020, *Proc. SPIE*, **11444**, 1144431
 Knödseder, J., Mayer, M., Deil, C., et al. 2016a, *A&A*, **593**, A1
 Knödseder, J., Mayer, M., Deil, C., et al. 2016b, Ctools: Cherenkov Telescope Science Analysis Software, Astrophysics Source Code Library, ascl:1601.005
 Komissarov, S. S. 2013, *MNRAS*, **428**, 2459
 Kotera, K., Phinney, E. S., & Olinto, A. V. 2013, *MNRAS*, **432**, 3228
 Kozyreva, A., Gilmer, M., Hirschi, R., et al. 2017, *MNRAS*, **464**, 2854
 Kuncarayakti, H., Maeda, K., Ashall, C. J., et al. 2018, *ApJL*, **854**, L14
 Levan, A. J., Read, A. M., Metzger, B. D., Wheatley, P. J., & Tanvir, N. R. 2013, *ApJ*, **771**, 136
 Li, T.-P., & Ma, Y.-Q. 1983, *ApJ*, **272**, 317
 Lunnan, R., Chornock, R., Berger, E., et al. 2018, *ApJ*, **852**, 81
 Lyubarsky, Y. E. 2003, *MNRAS*, **345**, 153
 Maier, G., & Holder, J. 2017, *Proc. ICRC (Busan)*, **301**, 747
 Margalit, B., & Metzger, B. D. 2016, *MNRAS*, **461**, 1154
 Margalit, B., Metzger, B. D., Berger, E., et al. 2018a, *MNRAS*, **481**, 2407
 Margalit, B., Metzger, B. D., Thompson, T. A., Nicholl, M., & Sukhbold, T. 2018b, *MNRAS*, **475**, 2659
 Margutti, R., Chornock, R., Metzger, B. D., et al. 2018, *ApJ*, **864**, 45
 Mauerhan, J. C., Filippenko, A. V., Zheng, W., et al. 2018, *MNRAS*, **478**, 5050
 McCrum, M., Smartt, S. J., Rest, A., et al. 2015, *MNRAS*, **448**, 1206

- Metzger, B. D., Margalit, B., Kasen, D., & Quataert, E. 2015, *MNRAS*, **454**, 3311
- Metzger, B. D., Vurm, I., Hascöet, R., & Beloborodov, A. M. 2014, *MNRAS*, **437**, 703
- Milisavljevic, D., Margutti, R., Kamble, A., et al. 2015, *ApJ*, **815**, 120
- Milisavljevic, D., Patnaude, D. J., Chevalier, R. A., et al. 2018, *ApJL*, **864**, L36
- Moriya, T. J., Maeda, K., Taddia, F., et al. 2013, *MNRAS*, **435**, 1520
- Moriya, T. J., Metzger, B. D., & Blinnikov, S. I. 2016, *ApJ*, **833**, 64
- Moriya, T. J., Nicholl, M., & Guillochon, J. 2018, *ApJ*, **867**, 113
- Murase, K., Franckowiak, A., Maeda, K., Margutti, R., & Beacom, J. F. 2019, *ApJ*, **874**, 80
- Murase, K., Kashiyama, K., Kiuchi, K., & Bartos, I. 2015, *ApJ*, **805**, 82
- Murase, K., Thompson, T. A., Lacki, B. C., & Beacom, J. F. 2011, *PhRvD*, **84**, 43003
- Nicholl, M. 2018, *RNAAS*, **2**, 230
- Nicholl, M., Berger, E., Blanchard, P. K., Gomez, S., & Chornock, R. 2019, *ApJ*, **871**, 102
- Nicholl, M., Berger, E., Margutti, R., et al. 2016a, *ApJL*, **828**, L18
- Nicholl, M., Berger, E., Smartt, S. J., et al. 2016b, *ApJ*, **826**, 39
- Nicholl, M., Blanchard, P. K., Berger, E., et al. 2018, *ApJL*, **866**, L24
- Nicholl, M., Blanchard, P. K., Berger, E., et al. 2020, *NatAs*, **4**, 893
- Nicholl, M., Berger, E., Margutti, R., et al. 2017a, *ApJL*, **845**, L8
- Nicholl, M., Guillochon, J., & Berger, E. 2017b, *ApJ*, **850**, 55
- Nicholl, M., Smartt, S. J., Jerkstrand, A., et al. 2013, *Natur*, **502**, 346
- Nicholl, M., Williams, P. K. G., Berger, E., et al. 2017c, *ApJ*, **843**, 84
- Nievas Rosillo, M. 2021, *Proc. ICRC (Berlin)*, **37**, 721
- Nolan, P. L., Abdo, A. A., Ackermann, M., et al. 2012, *ApJS*, **199**, 31
- Observatory, C. T. A., & Consortium, C. T. A. 2016, CTAO Instrument Response Functions—Version Prod3b-V2, Zenodo, doi:10.5281/Zenodo.5163273
- Park, N. 2015, *Proc. ICRC (The Hague)*, **34**, 771
- Planck Collaboration, Ade, P. A. R., Aghanim, N., et al. 2016, *A&A*, **594**, A13
- Pooley, D., Lewin, W. H. G., Fox, D. W., et al. 2002, *ApJ*, **572**, 932
- Prajs, S., Sullivan, M., Smith, M., et al. 2017, *MNRAS*, **464**, 3568
- Price-Whelan, A. M., Sipőcz, B. M., Günther, H. M., et al. 2018, *AJ*, **156**, 123
- Quataert, E., & Kasen, D. 2012, *MNRAS*, **419**, L1
- Quimby, R. M., Cia, A. D., Gal-Yam, A., et al. 2018, *ApJ*, **855**, 2
- Quimby, R. M., Kulkarni, S. R., Kasliwal, M. M., et al. 2011, *Natur*, **474**, 487
- Renault-Tinacci, N., Kotera, K., Neronov, A., & Ando, S. 2018, *A&A*, **611**, A45
- Robitaille, T. P., Tollerud, E. J., Greenfield, P., et al. 2013, *A&A*, **558**, 33
- Rolke, W. A., López, A. M., & Conrad, J. 2005, *NIMPA*, **551**, 493
- Smith, N., & Owocki, S. P. 2006, *ApJL*, **645**, L45
- Smith, N., Li, W., Foley, R. J., et al. 2007, *ApJ*, **666**, 1116
- Sorokina, E., Blinnikov, S., Nomoto, K., Quimby, R., & Tolstov, A. 2016, *ApJ*, **829**, 17
- Steinberg, E., & Metzger, B. D. 2018, *MNRAS*, **479**, 687
- Sukhbold, T., & Woosley, S. E. 2016, *ApJL*, **820**, L38
- The CTA Consortium 2019, Science with the Cherenkov Telescope Array (Hackensack, NJ: World Scientific)
- The H.E.S.S. Collaboration 2016, *Sci*, **347**, 406
- Vurm, I., & Metzger, B. D. 2021, *ApJ*, **917**, 77
- Wang, S. Q., Wang, L. J., Dai, Z. G., & Wu, X. F. 2015, *ApJ*, **799**, 107
- Weekes, T. C., Badran, H., Biller, S. D., et al. 2002, *Aph*, **17**, 221
- Wood, M., Caputo, R., Charles, E., et al. 2017, *Proc. ICRC (Busan)*, **301**, 824
- Woosley, S. E. 2010, *ApJL*, **719**, L204
- Woosley, S. E., & Heger, A. 2012, *ApJ*, **752**, 32
- Xi, S.-Q., Liu, R.-Y., Wang, X.-Y., et al. 2020, *ApJL*, **896**, L33
- Yan, L., Lunnan, R., Perley, D. A., et al. 2017, *ApJ*, **848**, 6
- Yan, L., Quimby, R., Ofek, E., et al. 2015, *ApJ*, **814**, 108
- Yuan, Q., Liao, N.-H., Xin, Y.-L., et al. 2018, *ApJL*, **854**, L18
- Zdziarski, A. A., & Svensson, R. 1989, *ApJ*, **344**, 551